

# Coupled Parametric Effects on Magnetic Fields of Eddy-Current Induced in Non-Ferrous Metal Plate for Simultaneous Estimation of Geometrical Parameters and Electrical Conductivity

Kok-Meng Lee<sup>1,2</sup>, *Fellow, IEEE/ASME*, Chun-Yeon Lin<sup>1</sup>, *Member, IEEE/ASME*, Bingjie Hao<sup>2</sup>, Min Li<sup>1</sup>

<sup>1</sup>George W. Woodruff School of Mechanical Engineering, Georgia Inst. of Tech., Atlanta, GA 30332, USA

<sup>2</sup>State Key Lab. of Digital Manufacturing Equipment and Technology, Huazhong Univ. of Sci. and Tech., Wuhan, Hubei, China

**Illustrated with a magnetic-field based eddy-current (EC) sensor which utilizes an anisotropic magneto-resistive (AMR) sensor to directly measure the magnetic flux density (MFD) generated by the EC induced in a non-ferrous metal plate, this paper presents a material-independent method for multi-objective estimation of the plate geometrical parameters and/or electrical conductivity using frequency response analysis. The model, which agrees well with a 2D axis-symmetric finite-element analysis, relates the measured (EC-generated) MFD to three dimensionless parameters (skin-depth, plate thickness and sensor-plate distance) normalized relative to a specified coil design. Data in the material-independent model that provides the basis to investigate the parametric effects on measured MFD can be regrouped in two-dimensional (2D) maps for simultaneously measuring any two of the three parameters. Experimental measurements were conducted on three different materials (Aluminum, Titanium and Titanium alloy) with different thicknesses and sensor-plate distances between 1 and 5mm operating in the frequency range from 100 Hz to 42.8 kHz. Experimental results show that the maximum difference between the analytically computed and experimental data is in the order of 5%, and demonstrate that the method has the capability of simultaneously measuring two unknowns out of three geometrical and/or material properties using a material-independent 2D map.**

**Index Terms**—Eddy current testing, eddy-current sensor, magnetic frequency response, geometrical measurements, electrical conductivity.

## I. INTRODUCTION

ESTIMATION of the geometry and material properties of a electrically conductive plate plays an important role in many applications, especially in the field of manufacturing. This trend is further motivated by the enormous surge of industrial interests in metallic additive manufacturing. Despite these potentials, questions remain about process reliability of the finished-part geometry and material properties, which require layer-by-layer defect detection as well as post-process precision machining. Motivated by these needs, this paper explores a mathematical framework for developing new eddy-current (EC) sensing methods capable of monitoring not only the plate displacement and thickness but also the variation its electrical conductivity while fabricating a component.

EC sensing has been in commercial use as a key non-destructive testing for inspecting electrically high-conductive materials, for examples [1]–[4] since 1950s, and is also commonly used technique for measuring thickness [5][6][7] and electrical conductivity [5][8][9][10]. Due to its simple structure and many advantages (such as long-term reliability, wide measuring range, fast response, high sensitivity and resolution, better anti-interference property, and insensitivity to oil or other media), it is expected that future EC sensors will play an increasingly important role in modern manufacturing [11][12] where real-time simultaneous measurements of multiple parameters are highly desirable. Conventionally, EC sensors are based primarily on two designs to measure EC effects; namely, the characteristic impedance of the excitation coil [5], and induced voltage in a secondary coil [2]. These traditional methods operated on the principle of inductive pick-up relying on high-frequency inputs to make a geometrical measurement generally have good linearity but

suffer decreasing sensitivity at lower frequencies. More recently, high-precision magnetic sensors with several advantages (including small-size, low-power consumption and fast-response) offer the ability to fulfill requirements at both high and low frequencies while ensuring the compact structure integrity of eddy current sensors. Several sensor types, such as Hall-effect sensor [6], anisotropic magneto-resistive (AMR) [12] and giant magneto-resistance (GMR) sensors [7][13][14][15], and superconducting quantum interference device (SQUID) [16][17] have been utilized in the designs.

Almost all the existing commercial EC sensors provide a single-function measurement; either one of the two geometrical (distance, thickness) parameters or the electrical conductivity. Significant research efforts have recently been directed towards simultaneous measurements by using special excitations instead of traditional single-frequency sinusoidal signal; for examples, pulsed [2][16][18] and multi-frequency [2][4][11] eddy-current techniques. The pulsed eddy-current techniques have the ability to contain nearly all frequencies but suffer several drawbacks including low signal-to-noise ratio (SNR). Although the techniques using multi-frequency excitation signals can significantly improve the SNR by choosing appropriate frequencies, they impose stringent requirements on hardware; for instance, excitation signals of very high frequency are required for distance measurements. For geometrical measurements, traditional EC sensors rely on calibrations to ensure accuracy, which are material-dependent, complicated and time-consuming. Because the relationships between the geometrical/material parameters and the measured magnetic fields are highly coupled and spatially nonlinear, the potentials of EC sensors for manufacturing applications are underexploited.

For the above reasons, this paper presents a new EC sensing method with a material-independent model for multi-

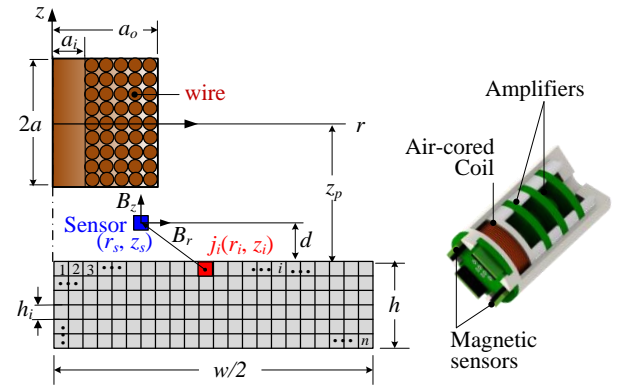
objective estimation of the geometrical parameters and/or electrical conductivity of non-ferrous metal plate. The focus here is the coupled parametric effects on the magnetic fields of the eddy-current induced in the non-ferrous metal plate using the axis-symmetric solutions [19] to illustrate and validate the method. To the best of our knowledge, this paper represents the first to use the classical solutions [19] as a material-independent model to simultaneously estimate two of three geometrical and/or material properties (skin-depth, plate-thickness and sensor-plate distance) using an eddy-current sensor based on magnetic field measurements. The remainder of this paper offers the following:

- A material-independent sensor model is illustrated with a Magnetic-field based Eddy-Current Sensor (MECS). Unlike traditional designs (that base inductive-impedance or voltage to make a measurement) which have a low sensitivity at lower frequencies, the MECS uses an AMR sensor to measure the magnetic flux density (MFD) generated by the EC induced in the conductive plate.
- The material-independent EC-MFD model derived with the aid of published solutions [19] relates the measured MFD to three dimensionless parameters that are normalized relative to the specified coil design; skin-depth  $\Delta$  (that characterizes the material and input frequency), conductive plate thickness  $H$ , and the sensor-plate distance  $Z_p$ . As will be shown, the model agrees well with a 2D axis-symmetric finite element analysis (FEA), and with experimental measurements conducted on two different materials (aluminum and titanium), each with four  $H$  and four  $Z_p$  values in the range of 100-25 kHz.
- The methods to derive 2D maps which can be calibrated from MFD measurements for simultaneous estimating any two of the three parameters ( $H$ ,  $Z_p$ ,  $\Delta$ ) are discussed. With the MECS dynamic model that accounts for the dynamics of both the EC-MFD system and the signal-processing circuits, the highly coupled and spatially nonlinear relationships between the geometrical/material parameters and measured MFD and its applications to multi-objective estimation are numerically illustrated and experimentally evaluated with several sets of quantitative measurements.

## II. FORMULATION OF MAGNETIC EDDY-CURRENT SENSOR

Figure 1 shows the CAD model of a Magnetic-field based Eddy-Current Sensor (MECS), and the coordinate system, parameters and variables for modeling the sensor. Placed above the non-ferrous electrically conductive plate, the MECS consists of an air-cored electromagnet (EM) (Fig. 1b) for inducing an eddy-current density (ECD) in the conductive plate, and a MFD-sensor with its associated power and signal processing circuits. When a sinusoidal current  $I_E(t) = I_o e^{j\omega t}$  flows through the EM, a steady state ECD  $\mathbf{J} e^{j\omega t}$  (where  $\mathbf{J} = \mathbf{J}_{\text{Re}} + j\mathbf{J}_{\text{Im}}$  is a 3D vector, and the subscripts “Re” and “Im” denote the real and imaginary parts respectively) is induced in the plate. For design purposes, the position coordinates and system geometries are normalized as follows:

$$R = \frac{r}{a_o}; Z = \frac{z}{a}; \rho_i = \frac{a_i}{a_o}; \rho_a = \frac{a}{a_o}; Z_p = \frac{z_p}{a} \text{ and } H = \frac{h}{a}$$



(a) EM and conductor (b) MECS CAD model  
Fig. 1 Schematics showing variables/parameters used in modeling

### A. Induced Eddy Current Density (ECD)

In terms of the dimensionless parameters, the analytical solution describing the ECD  $\mathbf{J}$  induced in the plate due to a harmonic-current-carrying EM with uniform current density  $J_o$  has been derived in widely accepted classical solutions [19] for an intermediate frequency range ( $f \leq 10^6$  Hz). For the large conductor ( $a_o \ll w/2$ ), the induced eddy-current is axis-symmetric:

$$\frac{J(R, Z)}{J_o} = j \frac{2}{\Delta_i^2} \int_0^\infty \left\{ \int_{\rho_i}^\psi \phi \beta_1(\phi) d\phi \right\} \chi(\psi) d\psi \quad (1)$$

$$\text{where } \Delta_i = \frac{\delta_i}{a_o} = \frac{1}{a_o} \sqrt{\frac{2}{\omega \sigma_i \mu_i}};$$

$$\chi(\psi) = \frac{\beta_1(\psi R) [D(Z_p - 1) - D(Z_p + 1)] [D_1(Z + Z_p + H) - 1]}{\psi^2 [( \psi + \psi_1 ) - ( \psi - \psi_1 ) D_1(H)]};$$

$$D(L) = \exp[\psi_1 \rho_a (Z + Z_p)] \exp(-\psi \rho_a L);$$

$$D_1(L) = \left( \frac{\psi_2 - \psi_1}{\psi_2 + \psi_1} \right) \exp(-2\psi_1 \rho_a L);$$

$$\text{and } \psi_i = \sqrt{\psi^2 + j \left( \frac{2}{\Delta_i^2} \right)}.$$

In (1),  $\sigma_i$  (where  $i = 1, 2$ ) are the conductivities of the 1<sup>st</sup> conductor with finite thickness  $h$  and the infinitely thick 2<sup>nd</sup> conductor;  $\beta_1(\phi)$  and  $\beta_1(\psi R)$  are the first-order Bessel equations; and  $\delta_i$  is the skin-depth. Without loss of generality, the following discussion assumes a non-ferrous conductor ( $\sigma_i \mu_i = \sigma \mu$ ) in contact with non-conductor in air.

For the cylindrical air-cored EM (Fig. 1b) with  $N_w$  turns of wire (diameter  $d_w$ ) wound between the inner and outer radii ( $a_i$  and  $a_o$ ) and length  $2a$ , the current density  $J_o$  can be written as

$$J_o = \left[ \frac{N_w I_E}{2a(a_o - a_i)} \right] \left[ \frac{N_w (\pi d_w^2 / 4)}{2a(a_o - a_i)} \right] \quad (2)$$

The second factor in (2) is an area-ratio accounting for the fact that the current only passes through the circular wires. The

current density can be simplified to (3) where  $C_E$  characterizes the winding geometry of the EM:

$$J_o = \frac{C_E I_o}{a_o a} \text{ where } C_E = \frac{\pi}{\rho_a} \left[ \frac{N_w D_w}{4(1-\rho_i)} \right]^2 \text{ and } D_w = \frac{d_w}{a_o} \quad (3)$$

As seen in (1), the axis-symmetric  $J(R, Z)$  for a given EM geometry ( $\rho_i$  and  $\rho_a$ ) depends on the conductor material and input frequency characterized by  $\Delta$ ; and conductor thickness  $H$ , and their relative location  $Z_p$ .

### B. MFD Measurement Model

Given the current density, the MFD at any point  $k$  in the neighborhood of the conductor can be derived from the Biot-Savart's law.  $\mathbf{B}(\mathbf{r}_k, t)$  can then be expressed in terms of discretized eddy-current as an output equation in (4) where  $\mathbf{B}_c$  and  $\mathbf{B}_e$  are the MFD contributed by the induced eddy-current in the conductor and by the EM respectively:

$$\mathbf{B}(\mathbf{r}_k, t) = [\mathbf{B}_r \quad \mathbf{B}_z]^T = \mathbf{B}_c + \mathbf{B}_e \quad (4)$$

To reduce the solutions to a tractable form, the conductive plate is discretized into  $n$  elements; each consists of an elemental eddy-current density  $\mathbf{j}_i$  flowing through area  $c_i$  (where  $i=1, 2, \dots, n$ ) as shown in Fig. 1(a):

$$\frac{\mathbf{B}_c(\mathbf{r}_k, t)}{B_o} = \frac{1}{B_o} \begin{bmatrix} B_{cr} \\ B_{cz} \end{bmatrix} = \begin{bmatrix} \eta_{cr}(\mathbf{r}_k) \\ \eta_{cz}(\mathbf{r}_k) \end{bmatrix} \mathbf{I}_c(t) \quad (5a)$$

$$\text{where } \mathbf{I}_c = \frac{1}{I_o} [\mathbf{j}_1 c_1 \quad \dots \quad \mathbf{j}_i c_i \quad \dots \quad \mathbf{j}_n c_n]^T; \quad (5b)$$

$$\begin{bmatrix} \eta_{cr} \\ \eta_{cz} \end{bmatrix} = \int_{\theta=0}^{2\pi} \begin{bmatrix} \rho_a (Z_k - Z_i) \cos \theta \\ (R_i - R_k \cos \theta) \end{bmatrix} \frac{R_i d\theta}{|\mathbf{R}_k - \mathbf{R}_i|^3}; \quad (5c)$$

$$|\mathbf{R}_k - \mathbf{R}_i| = \sqrt{(R_i - R_k \cos \theta)^2 + R_k^2 \sin^2 \theta + \rho_a^2 (Z_i - Z_k)^2}$$

$B_o = \mu_o I_o / (4\pi a_o)$ ;  $\mathbf{I}_c \in \mathbb{R}^{n \times 1}$ ;  $\eta_{cr}, \eta_{cz} \in \mathbb{R}^{1 \times n}$  with elements given in (5c); and  $\mu_o$  is the magnetic permeability of free space.

$\mathbf{B}_e$  is real and can be pre-computed numerically from (6a) where  $\eta_{Er}$  and  $\eta_{Ez}$  are scalar given in (6b):

$$\frac{\mathbf{B}_e(\mathbf{r}_k, t)}{B_o} = \frac{1}{B_o} \begin{bmatrix} B_{er} \\ B_{ez} \end{bmatrix} = C_E \begin{bmatrix} \eta_{Er}(\mathbf{r}_k) \\ \eta_{Ez}(\mathbf{r}_k) \end{bmatrix} \frac{I_E(t)}{I_o} \quad (6a)$$

where

$$\begin{bmatrix} \eta_{Er} \\ \eta_{Ez} \end{bmatrix} = \int_{\theta=0}^{2\pi} \int_{z=-1}^1 \int_{r=\rho_i}^{\rho_a} \begin{bmatrix} \rho_a (Z_k - Z) \cos \theta \\ (R - R_k \cos \theta) \end{bmatrix} \frac{R dR dZ d\theta}{|\mathbf{R}_k - \mathbf{R}|^3}; \quad (6b)$$

The solution (4) with components given in (5a-c) and (6a, b) relates the ECD-generated MFD ( $\mathbf{B}_e$ ) to the system parameters ( $\Delta, H, Z_p$ ) for a given EM design. Its physical significance for multi-target measurements is best illustrated numerically, which will be discussed and experimentally validated in the next two sections.

## III. ILLUSTRATIVE NUMERICAL RESULTS

In this section, the models (4-6) referred to here as distributed current source (DCS) method are numerically illustrated and compared with finite-element analysis (FEA),

which serve as a basis for exploring the parametric effects on simultaneous measurements.

### A. Verification of the ECD and MFD fields

The parametric values used in the numerical comparison are shown in Fig. 2(a). The 6mm-radius coil (with aspect ratios of  $\rho_i=3/8$  and  $\rho_a=1/3$ ) is placed 3.5mm above a 5mm-thick plate that has a width of 8 times larger than the coil radius justifying the axis-symmetric assumption for computing the eddy-current induced in the plate. The eddy-current solutions (1) were numerically integrated and discretized into distributed current sources (DCSs) so that the MFD measurements can be simulated using (4-6); for this, the plate is divided into equal-size (1mm<sup>2</sup>) square-elements as illustrated in Fig. 2(a). The MFD measurements were numerically simulated along a radial path (0.1mm increment) at 1mm height above the plate.

Fig. 2(b) shows the 2D FEA meshes (with triangular shaped elements) used in this study, which were automatically generated in a commercial FEA package COMSOL. Unlike the analytical solutions (1) and DCS-based MFD computation, FEA computes the magnetic vector potential and MFD fields of the EM and induced eddy-current in the WP; thus, it must enclose sufficiently large air-space around the EM and the conducting plate.

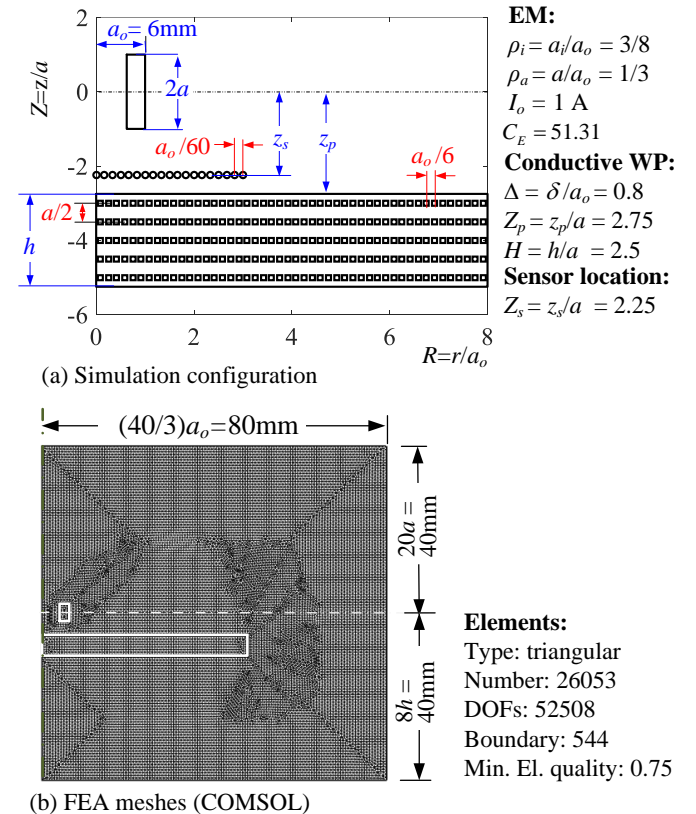


Fig. 2 Schematics illustrating parameters used in simulation

Figures 3(a-c) compare the results with FEA and the MFD directly computed from the curl of the magnetic vector potentials [19]:

- Fig. 3(a) shows the EM-generated ( $B_{er}$ ,  $B_{ez}$ ) computed from (6a, b), which agree excellently well with FEA. Both solutions are real as expected.
- The MFD generated by the opposing eddy-current density, ( $-B_{er}$ ,  $-B_{ez}$ ), were computed from (5a~c) with the ECD solutions numerically integrated from (1). As shown in Figs. 3(b) and 3(c) where the  $r$  and  $z$  components are plotted respectively, the real parts of the solutions agree well with FEA. However, the imaginary part of the FEA solutions are “noisy”. The “computation noise” depends on the mesh resolution of the FEA model and on the enclosing volume of the air space.
- Unlike  $B_{er}$  that has a bell-like curve (Fig. 3b) with a peak around  $R=1$ ,  $B_{ez}$  declines from  $R=0$  monotonically (Fig. 3c). As it can be uniquely characterized by a function of  $R$ , it is chosen for use in the subsequent measurements. In practice,  $B_{ez}$  can be obtained by subtracting  $B_{er}$  from the measured  $B_z$ .

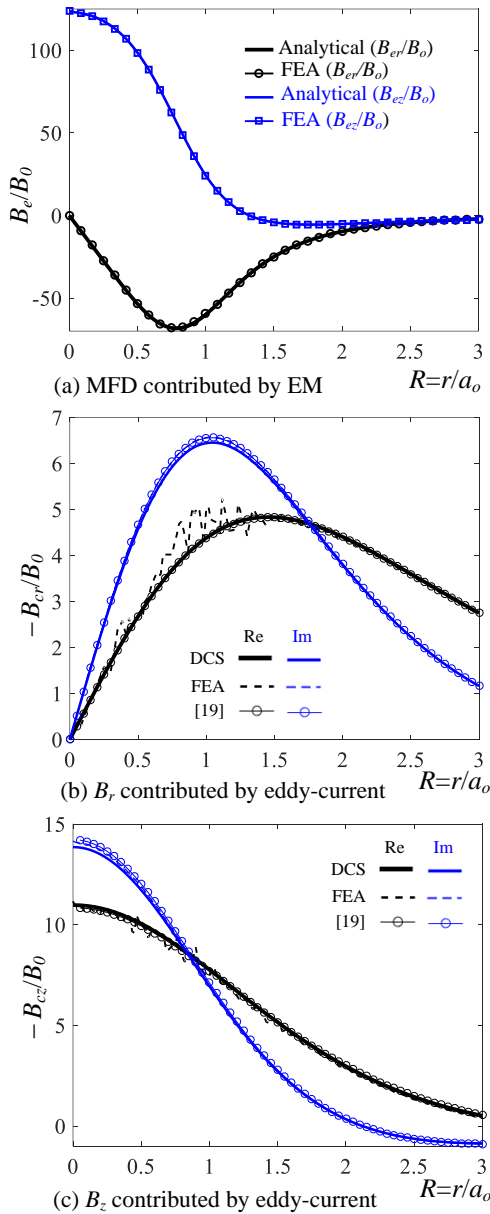


Fig. 3 Simulated MFD measurements for design in Fig. 2

## B. Parametric Effects on MECS

For a given EM/conductive-plate configuration,  $B_{cz}/B_o$  is a function of the normalized skin-depth  $\Delta$  (that depends on conductor material and input frequency), conductor thickness  $H$  and relative plate-location  $Z_p$ . The parametric effects on  $B_{cz}$  for the same configuration ( $\rho_r=3/8$ ,  $\rho_o=1/3$ , and  $H=2.5$ ) as in Fig. 2(a) are illustrated in Figs. 4 and 5 where  $B_{cz}$  is expressed in polar form (or magnitude and phase):

$$|B_{cz}| = \sqrt{B_{czRe}^2 + B_{czIm}^2} \text{ and } \angle B_{cz} = \tan^{-1}(B_{czIm} / B_{czRe}) \quad (7a,b)$$

Fig. 4(a) graphs 25 curves grouped into 5 families (or 5 values of  $Z_p$  ranging from 2.75 to 4.75 in step of 0.5) in the 3D plot that relates the normalized magnitude and phase (in degrees) of  $B_{cz}$  to  $\Delta$  (in  $\log_{10}$  scale). Each constant- $Z_p$  family is made up of 5 curves characterized by five  $H$  values (ranging from 0.5 to 2.5 in step of 0.5). To help visualize, the relationship between  $\Delta$  and  $|B_{cz}|$  and that between  $\Delta$  and  $\angle B_{cz}$  are plotted in 2D in Figs. 4(b) and 4(c) respectively. Fig. 5 graphs the plan view of the 3D plots in Fig. 4(a).

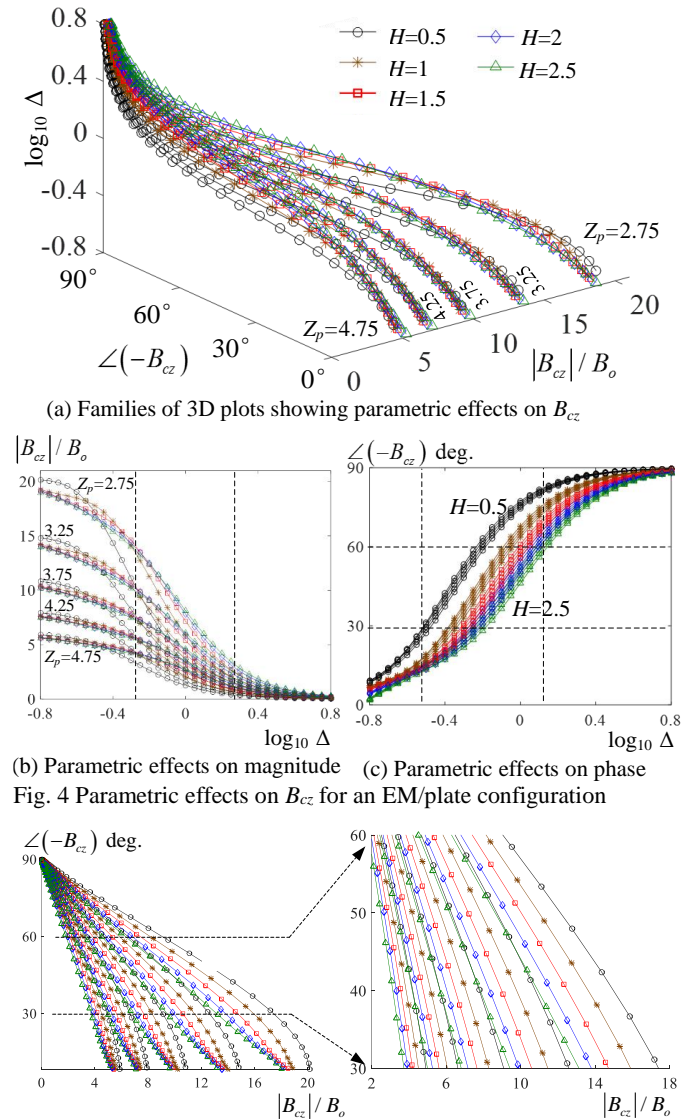


Fig. 5 Plan view (magnitude-phase) of the 3D plots in Fig. 4(a)

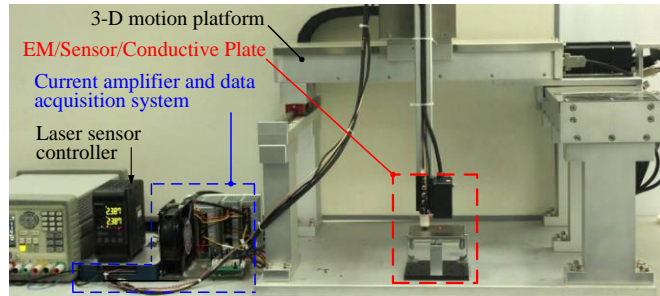


Some physically intuitive insights can be gained from Figs. 4 and 5 for optimizing a MECS design:

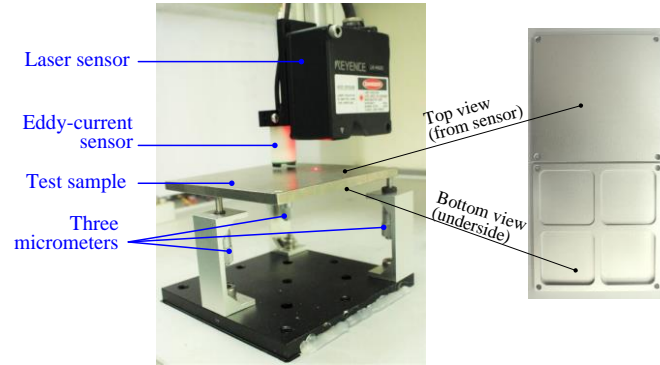
- Fig. 4(a) shows that when  $\log_{10} \Delta$  has a value between  $-0.8$  and  $0.8$ ,  $B_{cz}$  depends on both  $H$  and  $Z_p$ . Additionally,
 
$$\angle B_{cz} \rightarrow \begin{cases} 0^\circ & \text{when } \log_{10} \Delta < -0.8 \\ 90^\circ & \text{when } \log_{10} \Delta > 0.8 \end{cases}$$
- As shown in Fig. 4(b, c), both  $|B_{cz}|$  and  $\angle B_{cz}$  change with  $\log_{10} \Delta$ . However,  $|B_{cz}|$  is more sensitive to the change in the EM/conductor spacing  $Z_p$  while the family of five different  $Z_p$  values collapses into a single curve for a specified  $H$  suggesting that  $\angle B_{cz}$  depends primarily on  $H$ .
- The  $B_{cz}$  magnitude-phases plots (Fig. 5) show the plan-view of Fig. 4(a). Each curve represents a  $(H, Z_p)$  pair for the given  $\Delta$  values. The zoom-in view reveals that the curves are distinctive in the region  $30^\circ \leq \angle B_{cz} \leq 60^\circ$  corresponding to  $-0.5 \leq \log_{10} \Delta \leq 0.1$  (Fig. 4c).

#### IV. EXPERIMENTAL RESULTS AND DISCUSSION

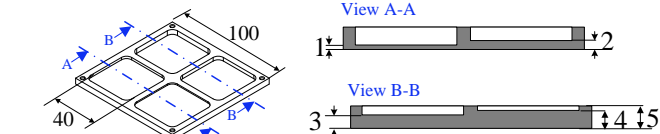
Fig. 6 shows the experimental setup for validating the EC sensor model. Three different materials were used in this study; Aluminum (Al), Titanium (Ti) and Titanium alloy (TC4).



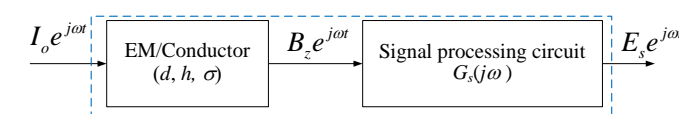
(a) Experimental testbed



(b) Measurement setup



(c) Test sample (dimensions in mm)



(d) Block diagram illustrating the sensor system dynamics

Fig. 6 Eddy current sensor structure

#### A. Experimental Setup

In this study, one of the two commercial (HMC1051) anisotropic magnetic resistance (AMR) sensors housed in the EC sensor (Fig. 1b) was used to measure the MFD. The EC sensor was positioned by a three degree-of-freedom (DOF) precision translation stage with a laser-sensor. As illustrated in Fig. 6(b), the  $z$ -position of the test-sample relative to the magnetic sensor can be fine-tuned by three micrometers and the laser-sensor to ensure that the test sample is parallel to the sensor  $xy$ -plane. Machined from a 5mm-thick 100mm-width square block, the test-sample consists of four square-pockets of different thicknesses (1, 2, 3 and 4mm) as geometrically shown in Fig. 6(c). Three materials (compared in Fig. 7) were used in this study; Al, Ti and TC4). The parametric values of the experimental setup are detailed in Table 1, where the transfer function of the sensor system was experimentally estimated. The conductivities of the samples were calibrated with a commercial conductivity-meter (Sigma 2008A). Measured with a micrometer, the actual thicknesses of the test samples were the average of three measurements over the  $40 \times 40 \text{ mm}^2$  region (TABLE I). Geometrically, the 3mm- and 4mm-thick Ti test-samples exhibit more uniformly accurate machined thickness than Al samples because of its significantly higher mechanical strength. However, the difficulty in machining thin-plates with a very small thickness-to-width ratio, along with that fact that Ti is well-known hard-to-machine material, contributes to the relatively large machining errors in the 1mm- and 2mm-thick Ti test-samples.

TABLE I. CHARACTERISTIC PARAMETERS OF EXPERIMENT SETUP

EM Coil ( $N_w = 60$ , $d_w = 0.35 \text{ mm}$ )	AMR Sensor (HMC1051ZL)
$(a_l, a_o, a) = (3.75, 6.5, 2) \text{ mm}$	Size: $6.5 \times 1.7 \times 2.0 \text{ mm}$
$I_o = 1 \text{ A}$ , $J_o = 4.27 \text{ A/mm}^2$ , $B_o = 16.67 \mu \text{ T}$	Position $(x_s, y_s, z_s)$ : $(6, 0, -4.5)$

#### 2D Map Calibration Samples

Aluminum (Al) sample	Titanium (Ti) sample
$\sigma_{\text{Al}} = 20.73 \text{ MSiemens/meter (MS/m)}$	$\sigma_{\text{Ti}} = 1.92 \text{ MS/m}$
$h = 1.091, 2.090, 3.136, 4.088 \text{ (mm)}$	$h = 0.909, 1.901, 2.997, 3.998 \text{ (mm)}$

#### Test Samples

Titanium (Ti)	Titanium alloy (TC4)
$\sigma_{\text{Ti}} = 1.92 \text{ MS/m}$	$\sigma_{\text{TC4}} = 0.56 \text{ MS/m}$
$h = 1.531, 2.530, 3.530 \text{ (mm)}$	$h = 1.013, 2.002, 3.002 \text{ (mm)}$

Sensor system dynamics:  $|G_s(j\omega)| = 1.34$  and  $\angle G_s(j\omega) = -4.85^\circ$

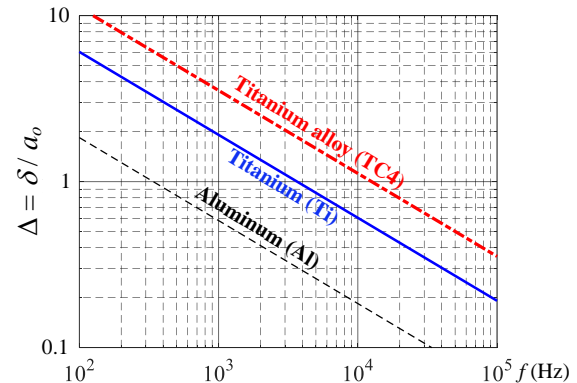


Fig. 7 Properties of Al, Ti and TC4

Frequency responses tests were conducted on three materials, Al, Ti and TC4, with an input frequency  $f$  ranging from 100 Hz to 42.8 kHz. The measured MFDs were sampled at a rate of 500 kHz using a commercial data-acquisition system (National Instruments, PXI-6255). Fig. 6(d) schematically illustrates the overall system dynamics: The 1<sup>st</sup> functional block represents the EM/conductive-plate system characterized by the parameters  $(d, h, \sigma)$ . The sensor dynamics contributed by the signal processing amplifiers and associated circuits are accounted for the transfer function  $G_s(j\omega)$  in the 2<sup>nd</sup> block.  $|G_s(j\omega)|$  and  $\angle G_s(j\omega)$  that characterize the sensor system dynamics were determined to be 1.34 and  $-4.85^\circ$  using a least-square (LS) method which minimizes the errors between the analytical solutions and experimental measurements. The 3mm and 4mm thick Ti samples, which have smallest average machining errors geometrically, were employed in this LS fit.

For investigating the parametric effects of the eddy-current, the MFD ( $B_{cz}$ ) in the absence of test-samples was measured during calibration so that the EM-generated MFD can be subtracted off from the measured MFD to determine the MFD components solely by the eddy-current induced in the conductor. The measured magnitude and phase are then scaled by  $|G_s(j\omega)|$  and shifted by  $\angle G_s(j\omega)$  respectively to eliminate the influence of the sensor dynamics in the measurements.

### B. Parametric Effects on Measured MFD

Figures 8 and 9 show the effects of the normalized distance  $Z_p$ , thickness  $H$  and skip-depth  $\Delta$  on the normalized magnitude (top) and phase (bottom) of the measured  $B_{cz}$  respectively. In these results, the phases are not plotted for cases where the magnitudes are too small ( $<20\mu\text{T}$ ) for reliable measurements.

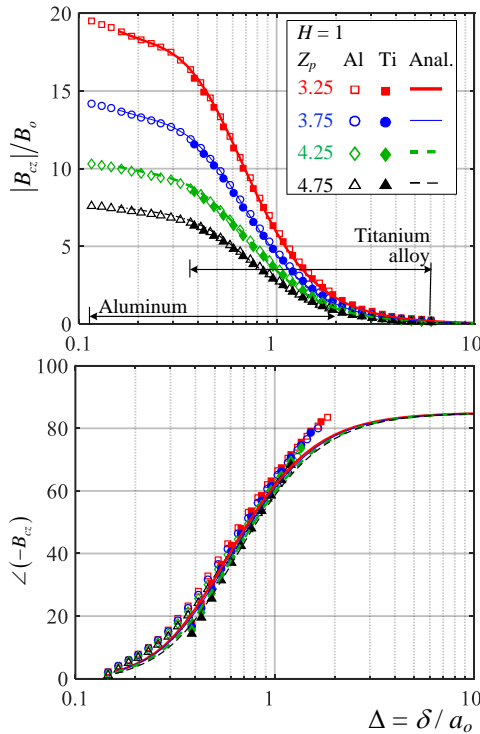


Fig. 8 Effects of  $Z_p$  on  $B_{cz}$  for a specified  $H=1$

Some observations can be drawn from Fig. 8 and 9:

- Fig. 8 shows the effects of the skip-depth  $\Delta$  (material properties and frequency) on  $B_{cz}$  for four  $Z_p$  values at a specified thickness  $H=1$ . The data (magnitude or phase) obtained from the two different materials (Al and Ti) at each  $Z_p$  collapse into a single curve. The top plot shows four distinctive magnitude curves at small skin-depths, each for a specified  $Z_p$ , suggesting that  $Z_p$  has significant effects on the  $B_{cz}$  magnitude. On the other hand, the phase data in the bottom plot collapse approximately into a single curve showing that  $Z_p$  has little influences on the  $B_{cz}$  phase.
- Fig. 9 shows the parametric effects of  $\Delta$  on  $B_{cz}$  for four  $H$  values at  $Z_p=3.25$ . In contrast to Fig. 8 for different  $Z_p$ ,  $H$  has a similar degree of influences on both magnitude and phase curves in the range  $0.4 \leq \Delta \leq 1.6$ . As shown in Fig. 9, the magnitude curves are significantly less sensitive to  $H$  than to  $Z_p$ , particularly at small skin-depths. Unlike the phase curves in Fig. 8, the four phase curves for different  $H$  are relatively distinct, showing that  $H$  exhibits significantly greater influences on the phase curves of  $B_{cz}$  than  $Z_p$ .

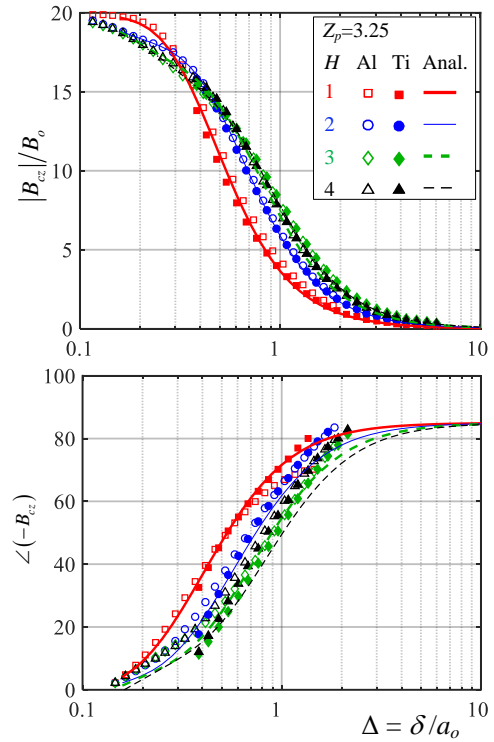


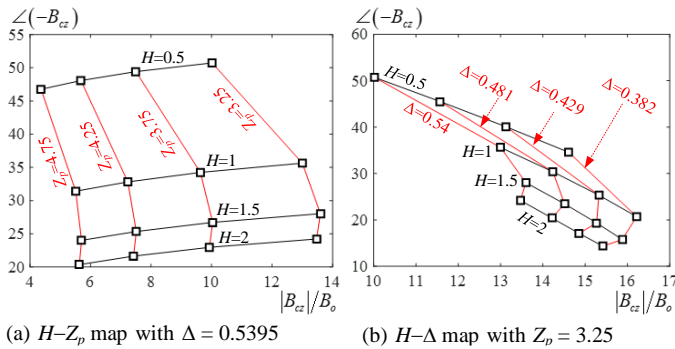
Fig. 9 Effects of  $H$  on  $B_{cz}$  for a specified  $Z_p=3.25$

### C. Experimental Validation

The experimental (magnitude, phase) data in Figs. 8 and 9 are regrouped into constant- $H$  and constant- $Z_p$  lines for a given  $\Delta$ ; the result is a two-dimensional (2D)  $H$ - $Z_p$  map as shown in Fig. 10(a). Similarly, a 2D-map relating  $H$  and  $\Delta$  for a specified  $Z_p$  can be obtained as shown in Fig. 10(b). These 2D maps, which can be calibrated from measured  $B_{cz}$  of a conductive workpiece, provide a basis for simultaneous estimates of  $(H, Z_p)$  with a known  $\Delta$ , or  $(H, \Delta)$  at a given  $Z_p$ .

To illustrate the applications of the model, the Ti sample is used in this illustration. Titanium plates with small thicknesses are commonly used in aerospace and biomedical industries because of its desirable properties including high strength-to-

weight ratio and good biocompatibility and resistance to corrosion. Ti has a low electrical conductivity of  $1.92 \times 10^6 \text{ S/m}$ , which is only 0.09 time of that of Aluminum. The low electrical conductivity presents a challenge to simultaneous  $(H, Z_p)$  measurements of a Ti workpiece using EC sensors during machining. The former needs a high-frequency current to induce a shallow skin effect near the surface independent of thickness. On the other hand, the latter relies on a low-frequency current to ensure a full penetration.



(a)  $H$ - $Z_p$  map with  $\Delta = 0.5395$   
Fig.10 Examples of 2D maps

Using Figs. 8 and 9 as a guide, an intermediate frequency of 12.59 kHz (corresponding to  $\Delta = 0.5395$ ) was chosen as a trade-off between high eddy-current effects and large skin-depth for the Ti sample. To provide quantitative comparisons, the percentage differences between the analytical and experimental magnitudes and phases are defined as follows:

$$\frac{|B_{cz}|_{\text{Exp}} - |B_{cz}|_{\text{Anal}}}{|B_{cz}|_{\text{Anal}}} \times 100\%, \quad \frac{[\angle B_{cz}]_{\text{Exp}} - [\angle B_{cz}]_{\text{Anal}}}{[\angle B_{cz}]_{\text{Anal}}} \times 100\%$$

Fig. 11 compares the experimentally obtained  $H$ - $Z_p$  map with analytically simulated results using actual thicknesses. Fig. 12 simulates the effect of  $\Delta$  variation (approximately 11% from  $\Delta = 0.5395$ ) on the  $(H, \Delta)$  map. Quantitative differences between analytical and experimental results are summarized in TABLES II and III; the % difference is well within 6%.

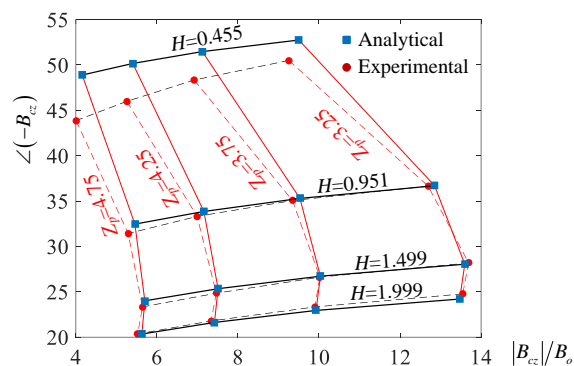


Fig. 11 Experimental validation, Ti at  $\Delta = 0.5395$

TABLE II. % DIFF. FOR DATA COMPARISON IN FIG. 11 ( $\Delta = 0.54$ )

$H$	$Z_p = 3.25$	$Z_p = 3.75$	$Z_p = 4.25$	$Z_p = 4.75$
0.455	5.15, 3.97	5.02, 4.14	4.89, 4.33	4.78, 4.52
0.951	1.12, 2.96	1.05, 3.07	0.99, 3.20	0.94, 3.33
1.499	0.00, 0.02	0.00, 0.02	0.00, 0.02	0.00, 0.02
1.999	0.00, 0.02	0.00, 0.02	0.00, 0.02	0.00, 0.03

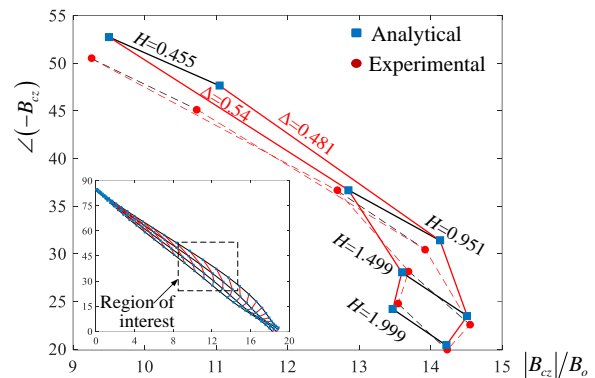


Fig.12 Experimental validation, Ti at  $Z_p = 3.25$

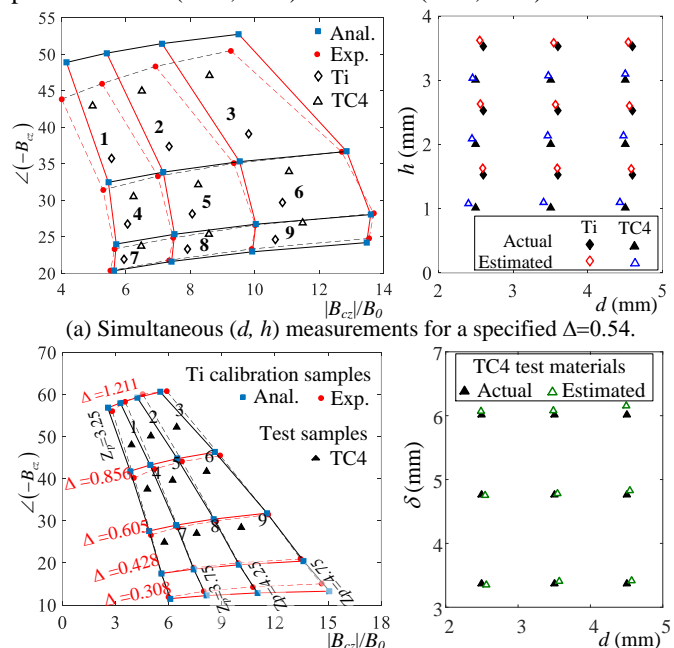
TABLE III. % DIFF. FOR DATA COMPARISON IN FIG. 12. ( $Z_p = 3.25$ )

$\Delta$	$H = 0.4545$	$H = 0.9505$	$H = 1.4985$	$H = 1.999$
0.540	2.58, 4.28	1.23, 0.13	0.71, 0.47	0.56, 2.33
0.481	2.89, 5.22	1.45, 3.02	0.26, 3.86	0.09, 2.42

### D. Illustrative Applications and Experimental Evaluation

Three sets of experiments were conducted to illustrate the material-independent method to estimate two unknowns out of the three  $(d, h, \delta)$  parameters using a two-dimensional (2D) linear interpolation mapping [20] outlined in Appendix. Two materials, Titanium (Ti) and Titanium alloy (TC4) with electrical conductivities of  $\sigma_{\text{Ti}} = 1.92$  and  $\sigma_{\text{TC4}} = 0.56 \text{ MS/m}$  respectively, 10 frequencies ranging from 5 to 42.8 kHz, 7 displacements and 7 thicknesses between 1mm and 5mm were used to evaluate the method experimentally.

The *first* and *second* sets simultaneously measured  $(d, h)$  of Ti and TC4 samples using the  $Z_p$ - $H$  map (Fig. 11) calibrated for Ti at 12.5 kHz. In each set, nine test samples with unknown  $(d, h)$  parameters were used. To maintain the specified  $\Delta = 0.54$ , the second set of the nine TC4 samples was conducted at 42.8 kHz. The results are graphically shown in Fig. 13(a) with their percentage errors listed in Table IV (non-shaded). The mean estimation errors (%) of the unknown  $(d, h)$  parameters are (1.11, 4.10) for Ti and (1.64, 5.28) for TC4.



(b) Simultaneous  $(d, \delta)$  measurements for a specified  $H = 2$ .

Fig. 13 Results of experimental evaluation



TABLE IV MEASUREMENT ERROR OF UNKNOWN PARAMETERS

	$\Delta=0.54$				$H = h / a = 2$ where $a=2$	
	$\sigma = 1.92 \text{ MS/m}$		$\sigma = 0.56 \text{ MS/m}$			
	$d, h \text{ (mm)}$	% Error	$d, h \text{ (mm)}$	% Error	$d, \delta \text{ (mm)}$	% Error
1	4.6, 1.531	0.79, 6.64	4.5, 1.013	1.49, 8.72	2.5, 6.018	0.344, 0.96
2	3.6, 1.531	0.50, 7.03	3.5, 1.013	2.57, 8.0	3.5, 6.018	0.265, 1.09
3	2.6, 1.531	0.52, 6.52	2.5, 1.013	3.97, 6.12	4.5, 6.018	0.062, 2.33
4	4.6, 2.53	1.09, 3.04	4.5, 2.002	0.43, 6.88	2.5, 4.758	1.805, 0.09
5	3.6, 2.53	1.11, 3.87	3.5, 2.002	1.01, 6.55	3.5, 4.758	1.368, 0.38
6	2.6, 2.53	1.40, 3.86	2.5, 2.002	1.91, 4.42	4.5, 4.758	0.975, 1.48
7	4.6, 3.53	1.25, 1.84	4.5, 3.002	0.03, 3.31	2.5, 3.366	2.557, 0.29
8	3.6, 3.53	1.67, 1.56	3.5, 3.002	0.78, 2.38	3.5, 3.366	1.900, 1.18
9	2.6, 3.53	1.61, 2.55	2.5, 3.002	2.51, 1.10	4.5, 3.366	1.600, 1.55
Average %	1.11, 4.10		1.64, 5.28		1.21, 1.04	
Std. Dev. %	0.43, 2.13		1.25, 2.61		0.85, 0.71	

To evaluate the method for simultaneously measuring both the displacement and skin-depth ( $d, \delta$ ) for a given  $H$ , a  $Z_p$ - $\Delta$  map for a Ti sample ( $H=2$ ) was calibrated with five different frequencies ( $f = 2.5, 5, 10, 20, 40\text{kHz}$ ) and four  $Z_p$  values (3.25, 3.75, 4.25, 4.75). As shown in the left plot of Fig. 13(b), the experimentally obtained  $Z_p$ - $\Delta$  map agrees well with the analytically simulated results. Using the linear interpolation mapping outlined in Appendix, the *third* set of the nine TC4 samples (with  $f=12.5, 20, 40\text{kHz}$  and  $Z_p=3.5, 4, 4.5$ ) demonstrates that the unknown ( $d, \delta$ ) values can be estimated from the  $Z_p$ - $\Delta$  map obtained with Ti samples. The results and measurement errors are summarized in Fig. 13(b) and Table IV (shaded column) respectively, which show a mean percentage error of (1.21, 1.04).

Fig. 13 and Table IV demonstrate that the method is material-independent and can simultaneously measure ( $d, h$ ) or ( $d, \delta$ ) parameters using the same  $Z_p$ - $H$  map or  $Z_p$ - $\Delta$  for different material samples. The electrical conductivity can be estimated from the measured skin-depth and excitation frequency. The average and standard deviation (Std. Dev.) of the estimated electrical conductivity for these nine test points are (0.5495, 0.0089) MS/m with a relative percentage error of 1.87 %.

## V. CONCLUSION

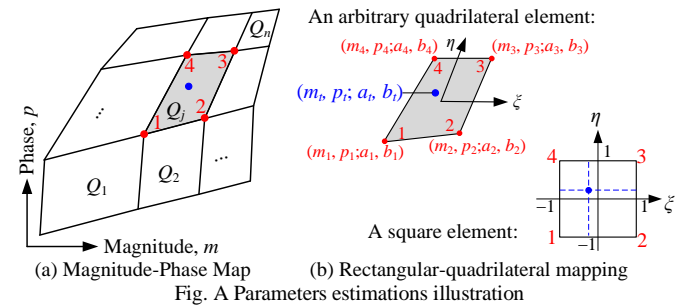
A material-independent model, which relates the measured (EC-generated) MFD to three characteristic parameters (skin-depth  $\Delta$ , plate thickness  $H$  and sensor-plate distance  $Z_p$ ) normalized relative to a specified coil design, has been presented for estimating any two of the three ( $\Delta, Z_p, H$ ) parameters of a non-ferrous metal plate. The model provides the basis for investigating the parametric effects on the measured magnitude and phase of the EC-generated MFD, both numerically and experimentally.

Validated with experiments conducted on the two materials (aluminum and titanium alloy) in the range of 100-25 kHz, the results confirm that the magnitude or phase of the MFD contributed by the EC-induced depends only on the normalized skin-depth (regardless of materials) for the specified pair of ( $H, Z_p$ ). The results also show that  $Z_p$  has a distinct effect on the ( $B_{cz}$  vs  $\Delta$ ) magnitude curves particularly for very small  $\Delta$ ; whereas  $H$ , on the other hand, exhibits

significantly greater influences than  $Z_p$  on the ( $B_{cz}$  vs  $\Delta$ ) phase curves. The material-independent model can be regrouped in 2D maps for simultaneously measuring any two of the three parameters. Comparisons between the analytically computed 2D maps and those calibrated experimentally show that the maximum difference is in the order of 5%. Simultaneous measurements of two unknowns out of three geometrical and/or material properties using material-independent 2D maps demonstrate the efficiency and accuracy of this method.

## APPENDIX

The inverse solutions that solve ( $a_i, b_i$ ) given the measured ( $m_i, p_i$ ) can be formulated as a  $2 \times 2$  mapping problem as illustrated in Fig. A. Each of the  $j^{\text{th}}$  quadrilateral element  $Q_j$  is formed by four calibrated points ( $m_i, p_i; a_i, b_i$  where  $i=1$  to 4), which is linearly mapped into to a square element in ( $\xi, \eta$ ) coordinates using linear interpolation functions (A.1) where  $-1 \leq (\xi, \eta) \leq 1$ .



The procedure consists of three steps. The 1<sup>st</sup> locates the local quadrilateral element  $Q_j$  within which the measured point ( $m_i, p_i$ ) is located as shown in Fig. A(a). Given ( $m_i, p_i$ ) in  $Q_j$ , the 2<sup>nd</sup> step solves the pair of nonlinear equations (A.1) for the corresponding ( $\xi, \eta$ ):

$$\begin{bmatrix} m_i \\ p_i \end{bmatrix} = \begin{bmatrix} m_1\psi_{--} + m_2\psi_{-+} + m_3\psi_{++} + m_4\psi_{+-} \\ p_1\psi_{--} + p_2\psi_{-+} + p_3\psi_{++} + p_4\psi_{+-} \end{bmatrix} \quad (\text{A.1})$$

where  $\psi_{\pm\pm} = 0.25(1 \pm \xi)(1 \pm \eta)$ . Since ( $m, p$ ) to ( $a, b$ ) is bijective, the 3<sup>rd</sup> step determines ( $a_i, b_i$ ) by means of a similar linear mapping:

$$\begin{bmatrix} a_i \\ b_i \end{bmatrix} = \begin{bmatrix} a_1\psi_{--} + a_2\psi_{-+} + a_3\psi_{++} + a_4\psi_{+-} \\ b_1\psi_{--} + b_2\psi_{-+} + b_3\psi_{++} + b_4\psi_{+-} \end{bmatrix} \quad (\text{A.2})$$

## ACKNOWLEDGMENT

This work was supported in part by the U. S. National Science Foundation EFRI-M3C 1137172, National Basic Research Program of China (973 Program Grant No. 2013CB035803), and Guangdong Innovative Research Team Program (No. 2011G006).

## REFERENCES

- [1] B. Lebrun, Y. Jayet, and J.-C. Baboux, "Pulsed Eddy Current Signal Analysis: Application to the Experimental Detection and Characterization of Deep Flaws in Highly Conductive Materials," *NDT&E International*, vol. 30, no. 3, pp. 163-170, 1997.
- [2] R. Grimberg, A. Savin, E. Radu, and O. Mihalache, "Nondestructive Evaluation of the Severity of Discontinuities in Flat Conductive Materials by an Eddy-Current Transducer with Orthogonal Coils," *IEEE Trans. on Magnetics*, vol. 36, no. 1, pp. 299-307, 2000.
- [3] M. Wrzuszczak and J. Wrzuszczak, "Eddy Current Flaw Detection with Neural Network Applications," *Measurement*, vol. 28, no.2, pp. 132-136, 2005.
- [4] Y. L. Diraison, P.-U. Joubert and D. Placko, "Characterization of Subsurface Defects in Aeronautical Riveted Lap-joints Using Multi-frequency Eddy Current Imaging," *NDT&E International*, vol. 42, no. 2, pp. 133-140, 2009.



- [5] John C. Moulder, Erol Uzal, and James H. Rose1, "Thickness and Conductivity of Metallic Layers from Eddy Current Measurements," *Review of Scientific Instruments*, vol. 63, no. 6, pp. 3455-3465, 1992.
- [6] D. G. Park, C. S. Angani, G. D. Kim, C. G. Kim, and Y. M. Cheong, "Evaluation of Pulsed Eddy Current Response and Detection of the Thickness Variation in the Strainless Steel," *IEEE Trans. on Magnetics*, vol. 45, no. 10, pp. 3893-3896, 2009.
- [7] J. Kral, R. Smid, H. Maria G. Ramos, and A. L. Ribeiro, "The Lift-off Effect in Eddy Current on Thickness Modeling and Measurement," *IEEE Trans. on Instrumentation and Measurement*, vol. 62, no. 7, pp. 2043-2049, 2013.
- [8] N. Bowler, and Y. Q. Huang, "Electrical Conductivity Measurement of Metal Plates using Broadband Eddy-Current and Four-Point Methods," *Measurement Sci. and Tech.*, vol. 16, no. 11, pp 2193-2200, 2005.
- [9] X. Ma, A. J. Peyton, and Y. Y. Zhao, "Measurement of the Electrical Conductivity of Open-celled Aluminum Foam Using Non-contact Eddy Current Techniques," *NDT&E International*, vol. 38, no. 5, pp 359-367, 2005.
- [10] X. Ma, and A. J. Peyton, "Eddy Current Measurement of the Electrical Conductivity and Porosity of Metal Foams," *IEEE Trans. on Instrumentation and Measurement*, vol. 55, no. 2, pp 570-576, 2006.
- [11] K.-M. Lee, M. Li and K. Bai, "An Investigation of Eddy-current Effects on Parameter Monitoring for Duplex Lathe Machining of thin-Wall Components," *ASME Dynamic Systems and Control Conf.*, San Antonio, Texas, USA, Oct. 22-24, 2014, DSCC2014-6193.
- [12] K.-M. Lee, C.-Y. Lin, M. Li, and B. J. Hao, "Harmonic Response of an Eddy-Current Sensor for Real-time Measurement of Thin-wall Titanium Alloy Workpiece," *IEEE/ASME AIM*. Banff, Canada, July 12-15, 2016, pp. 1271-1276.
- [13] T. Dogaru and S. T. Smith, "Giant Magnetoresistance-Based Eddy-Current Sensor," *IEEE Trans. on Magnetics*, vol. 75, no. 5, pp. 3831-3838, 2001.
- [14] M. Sakthivel, B. George, and M. Sivaprakasam, "A Novel GMR-based Eddy Current Sensing Probe with Extended Sensing Range," *IEEE Trans. on Magnetic*, vol. 52, no. 4, pp. 1-12, 2016.
- [15] G. Yang, A. Tamburrino, L. Udpa, S. S. Udpa, Z. Zeng, Y. Deng, and P. Que, "Pulsed Eddy-Current Based Giant Magnetoresistive System for the Inspection of Aircraft Structures," *IEEE Trans. Magnetics*, vol. 46, no. 3, pp 910-917, Mar., 2010.
- [16] J. R. Claycomb, N. Tralshawala and J. H. Miller, Jr., "Theoretical Investigation of Eddy-Current Induction for Nondestructive Evaluation by Superconducting Quantum Interference Devices," *IEEE Trans. on Magnetics*, vol. 35, no. 5, pp. 292-298, 2000.
- [17] T. Kiwa, H. Tahara, E. Miyake and H. Yamada, and Keiji Tsukada, "Non-contact Thickness Gauge for Conductive Materials Using HTS SQUID System," *IEEE Trans. on Applied Superconductivity*, vol. 19, no. 3, pp. 801-803, 2009.
- [18] G. Y. Tian, Y. Li, and C. Mandache, "Study of Lift-off Invariance for Pulsed Eddy-Current Signals," *IEEE Trans. on Magnetics*, vol. 45, pp. 184-191, 2009.
- [19] C. V. Dodd and W. E. Deeds, "Analytical Solutions to Eddy-Current Probe-Coil Problems," *J. Appl. Phys.*, vol. 39, pp. 2829-2838, 1968.
- [20] J. N. Reddy, *An Introduction to the Finite Element Method*, 3rd ed., McGraw Hill, pp. 526-570.